

# Pore size distribution effects on the thermal conductivity of light weight autoclaved aerated concrete

**ABSTRACT:** Aim of the present study was to correlate thermal conductivities of highly porous autoclaved aerated concrete (apparent density < 100 kg/m<sup>3</sup>) with appendant micro-and nano-structural properties. AAC specimens with approximate apparent densities, but different pore size distributions were fabricated through utilizing specially selected, surface active additives when preparing the slurry of raw materials, aluminum and water. The main focus of this study is on the quantitative analysis of size and morphology of both pores and solid skeleton by 3D X-ray tomography (CT) and scanning electron microscopy (SEM). Moreover, specific surface areas and pore size distributions were determined by the methods of gas adsorption and mercury porosimetry. Apparent thermal conductivities depend on the number of pores, pore size distributions and thicknesses of the separating walls of the solid skeleton. The present study provides further insight in the mechanisms of heat transfer in light weight autoclaved aerated concrete.

## 1. Introduction

### 1.1. Heat transfer in porous materials

Thermal conductivity depends on temperature, density, structure and chemical nature of the material. In AAC, it is largely a function of density and moisture content [1, 2]. Densely packed structures with a high degree of crystallinity involve high thermal conductivities. Heat transport in the solid phase is carried out via thermal vibrations (phonons) on atomic and/or molecular level. In the gaseous phase, thermal energy is transported via collisions among gas molecules. In a model of nanoscale heat transport, the most important factor is the ratio of the mean free path of the carriers (here phonons and/or gas molecules) to the length of the sample -the Knudsen number [3]. With respect to heat transport in the gaseous phase this phenomenon is known as Smoluchowsky-effect that occurs at pore diameters < 100 nm (under atmospheric pressure and air as the gas phase) [3]. Thus, especially in light weight AAC where the porosity may be higher than 90 %, thermal conductivity is closely connected with the amount of pores and their distribution [4].

## 2. Experimental

The light weight AAC insulation board YTONG Multipor® is a product of Xella Deutschland GmbH (Duisburg, Germany). It is manufactured from sand, cement, lime, gypsum, aluminium paste, water and inorganic fillers. YTONG Multipor boards have a compressive strength ≥ 300 kPa in conjunction with a declared thermal conductivity (23°C/50% rel. hum.) of 0,043 W/(mK) or a compressive strength ≥ 350 kPa in conjunction with a declared thermal conductivity (23°C/50%) of 0,045 W/(mK). Apparent densities are between 100 kg/m<sup>3</sup> and 115 kg/m<sup>3</sup> [5].

Additives Silres® SMK 2101 ("ORIG"), SMK 2101-TYPE 6 and SMK 2101-TYPE 29 were from Wacker Chemie AG (Burghausen, Germany). Silres SMK 2101 is a standard product. SMK 2101-TYPE 6 and TYPE 29 were R&D test samples provided by Wacker.

Apparent densities were determined according to the standard EN 12068:199706. Thermal conductivities λ<sub>10,dry</sub> were determined according to DIN EN 12667:2001-01 with a TLP-500P (TAURUS Instruments GmbH, Weimar, Germany) by heat flow measurements using the guarded hot-plate method. Compressive strengths were analyzed according to DIN EN 826:1996-05 with a universal testing machine (TONI Technik Baustoffprüfsysteme GmbH, Berlin, Germany). Mineralogical analyses were carried with an X'Pert PRO Materials Research Diffractometer by using X'Pert Quantify and X'Pert High Score Plus software (PANalytical GmbH, Kassel, Germany). X-ray computer tomography (CT) studies were performed on a CT-ALPHA 225 (ProCon X-ray GmbH, Garbsen, Germany) using a C74942SK-05 flat panel detector (Hamamatsu Photonics, Japan) and MAVI – Modular Algorithms for Volume Images V1.8.1 Software. Mercury porosimetry measurements were performed on a PASCAL 240/440 (Porotec, Hofheim, Germany). Specific surface areas were analyzed according the Brunauer, Emmet & Teller (BET) method (DIN 66132) using an AREA Meter II (Ströhlein Instruments, Viersen, Germany). SEM images were taken using a XL 30 (Philips, Netherlands). Samples were sputter coated with a few Å of carbon.

## 3. Results and discussion

### 3.1. Thermal, mechanical and mineralogical analysis

The mechanical and thermal properties of all investigated samples are given in Table 1. We calculated total porosities of 95–97% for

all samples. The sample w/o additive showed an apparent density of 117 kg/m<sup>3</sup>, whereas specimen prepared with SMK 2101-ORIG, SMK 2101-TYPE 6 and SMK TYPE 29 showed lower, but uniform densities between 90 and 96 kg/m<sup>3</sup>. (Observed discrepancies were caused by slightly differing recipes compositions and were not an effect of the additives). An elegant way to create a common basis of comparison is the calculation of relative strength levels that are independent from apparent densities – dimensionless “A-values”. This method employs the experimentally well proven potential function between compressive strength and apparent density in AAC [6], which is given in equation 1. From measured data sets we deduced rather typical A-values for light weight AAC/YTONG Multipor (MW = 1957, SD = ± 210). However, samples SMK 2101-TYPE 6 and TYPE 29 showed a trend towards slightly and lower relative strength, respectively.

Equation 1. Calculation of relative strength levels [6].

$$A\text{-value} = \sigma_{CP}/(\text{const.} \cdot \rho^2)$$

$\sigma_{CP}$  – compressive strength [N/mm<sup>2</sup>],

$\rho$  – dry density [g/cm<sup>3</sup>],

const. – 0.016 [N/g<sup>2</sup>].

The thermal conductivity of the control sample w/o additive was extrapolated by a method that was experimentally established for light weight AAC (100 to 115 kg/m<sup>3</sup>). For fitting towards lower apparent density values, a fixed value of 0,0001 W/(mK) is to be subtracted for each kg/m<sup>3</sup>. In consideration of this fitted control value (w/o additive) significant differences in thermal conductivities became obvious: Samples w/o additive and with SMK 2101ORIG exhibited equal values around 0,042 W/(mK). By contrast, test results for samples with SMK 2101-TYPE 6 and TYPE 29 revealed clearly reduced  $\lambda_{10,\text{dry}}$  values of 0,0409 W/(mK) and 0,0391 W/(mK), respectively.

Mineralogical analyses by X-ray powder diffraction revealed a similar content of crystalline phases in all four samples. The main reac-

Table 1

PROPERTIES OF SAMPLES W/O ADDITIVE, WITH SMK 2101-ORIG, SMK 2101TYPE 6 AND SMK 2101-TYPE 29.

	Apparent density [kg/m <sup>3</sup> ]	Compr. strength [kPa]	A-Number	Thermal cond. $\lambda_{10,\text{dry}}$ [W/(mK)]	Thermal cond. $\lambda_{10,\text{dry}}$ extr. 95 kg/m <sup>3</sup> [W/(mK)]
w/o additive	117,0	410	1872	0,0448 ± 0,0022	0,04265
SMK 2101-ORIG	93,0	290	2074	0,0425 ± 0,0005	–
SMK 2101-TYPE 6	95,0	310	2175	0,0409 ± 0,0002	–
SMK 2101-TYPE 29	93,0	236	1705	0,0391 ± 0,0003	–

Table 2

X-RAY DIFFRACTION OF SAMPLES W/O ADDITIVE, WITH SMK 2101ORIG, SMK 2101-TYPE 6 AND SMK 2101-TYPE 29.

	Amorphous	Anhydrite / Gypsum	Calcite	Hydroxylellestadit	Katoit	Quartz	Tobermorite 11 Å monoclinic	Tobermorite 11 Å ortho	Tobermorite 11 Å Total
w/o additive	10,33	7,75	26,48	3,26	3,19	1,95	14,17	32,86	47,03
SMK 2101ORIG	15,10	6,75	23,84	2,57	2,17	1,94	14,78	32,84	47,62
SMK 2101TYPE 6	18,86	7,64	18,03	-	5,28	1,92	12,44	35,83	48,27
SMK 2101TYPE 29	12,75	6,92	22,06	3,42	3,00	1,11	12,16	38,57	50,73

tion products belong to the tobermorite group of calcium silicate hydrates. Quartz contents were found to be below 2 M.-%. Sample SMK 2101-TYPE 6 showed a trend towards higher amorphous components content. Altogether, measured values for amorphous phases were in the typical range for YTONG Multipor (Table 2).

In summary, our results suggest that neither chemical/mineralogical compositions nor mass-to-volume-ratios are responsible for the diverging thermal properties. Yet, differences in the nano-and/or microstructures came into consideration and were consecutively investigated by the methods of gas adsorption, mercury intrusion porosimetry, X-ray computer tomography and scanning electron microscopy.

### 3.2. Gas adsorption analysis (BET) and mercury intrusion porosimetry (MIP)

Specific surface was measured using Brunauer, Emmett & Teller (BET) method of gas adsorption. The physical adsorption of gas (nitrogen) molecules on a solid surface serves as the basis for the determination of its specific surface area. The specific surface area is a result from the total number of nitrogen molecules (in a monomolecular layer) and their spatial requirement (equation 2). In comparison to the control w/o additive, all samples revealed distinct increases in specific surface area. This trend was higher for the sample prepared with SMK 2101-TYPE 6 (75% increase). It was less pronounced, but still visible in samples with SMK 2101-ORIG (increased of 20%) and SMK 2101-TYPE 29 (increased of 30%), respectively (Fig. 1. A).

Equation 2. BET equation.

$$\frac{\frac{p}{p_0}}{a\left(1-\frac{p}{p_0}\right)} = \frac{1}{a_m} C + C - \frac{1}{a_m} C \cdot \frac{p}{p_0}$$

where:

$p$  – equilibrium pressure,

$p_0$  – pressure of saturated vapour of adsorbate,

$a$  – total mass of adsorbed gas under the pressure  $p$ ,

$a_m$  – mass of gas adsorbed in monolayer,

$C$  – constant linked exponentially with the difference between the adsorption enthalpy in the first layer and enthalpy of adsorption in further layers.

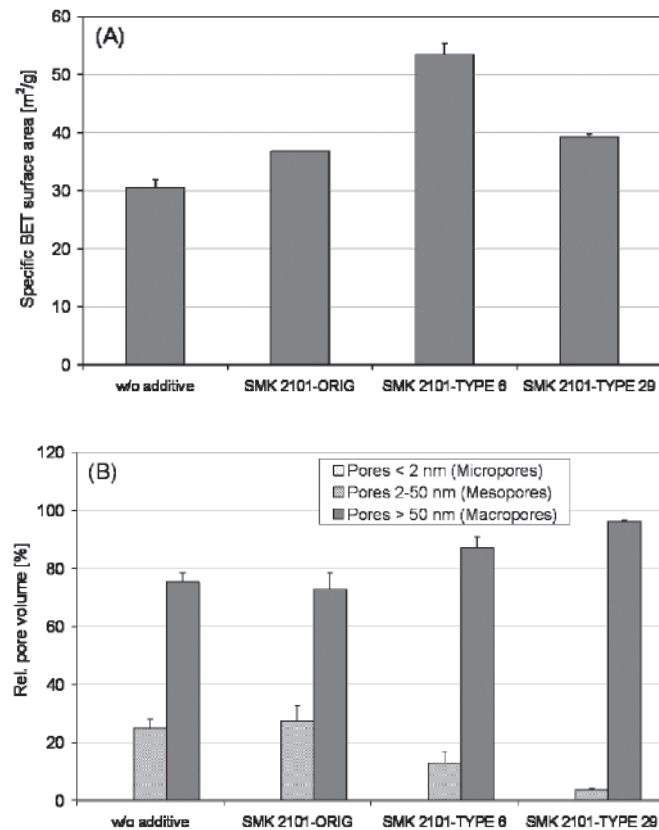


Fig. 1. (A) Specific BET surface areas. (B) Pore size distributions from mercury intrusion porosimetry (MIP) measurements.

The results of BET studies were complemented by mercury intrusion porosimetry (MIP) measurements. MIP analyses were carried out at a pressure of 200 MPa, which corresponds to a theoretical minimum pore diameter of 7.5 nm. The method is based on the capillary law governing the penetration of liquids into small spaces. In the case of a non-wetting liquid like mercury, this law is expressed by the Washburn equation (equation 3). On the basis of MIP results differential and integral pore size distributions were compiled [7]. Pores, which are larger than 100 µm in size, cannot be characterized by this method.

Equation 3. Washburn equation.

$$p = (2\gamma \cdot \cos \theta)/r$$

$p$  – applied pressure,

$r$  – pore radius,

$\theta$  – contact angle between Hg and sample,

$\gamma$  – Hg surface tension.

The results of the MIP are summarized in Figure 1 B. The detection of micropores (< 2 nm) via MIP is per se not possible. All four samples showed predominantly macropores (> 50 nm), this finding was particularly pronounced in samples SMK 2101-TYPE 6 and TYPE 29. The latter consisted virtually only of macropores (~ 96%). The pore size distribution of all investigated samples is bimodal, with one maximum in the mesoporous range (radii from 20–100 nm), and another one in the macroporous range (radii from 20 to 50 µm (Figure 2. A+B)). In all samples the first, mesoporous maximum was less pronounced than the second, macroporous one. It is worth mentioning that the intensity ratio 50 µm/50 nm increased from ~1.0 for the samples w/o additive and with 2101-ORIG, to ~1.8 and finally ~8.0 for the samples with SMK 2101-TYPE 6 and TYPE 29, respectively.

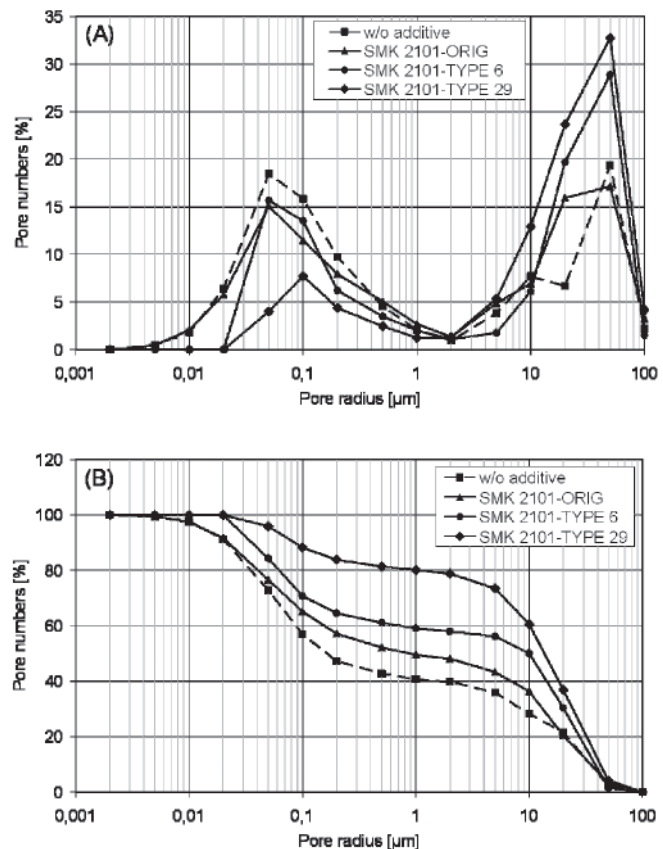


Fig. 2. (A) Differential and (B) integral pore size distributions (MIP). The dashed line corresponds to the control sample w/o additive.

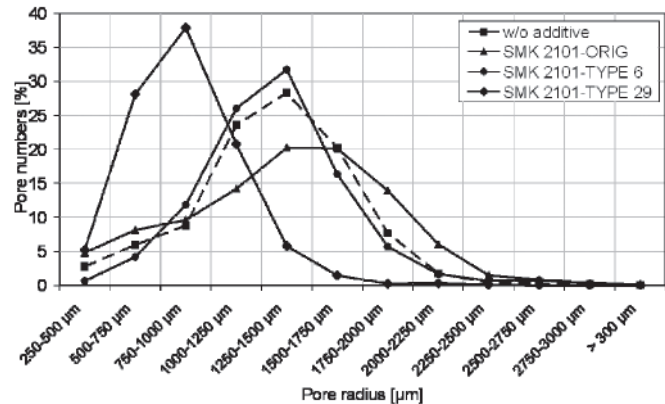


Fig. 3. Pore size distributions according to X-Ray CT. The dashed line corresponds to the control sample w/o additive.

### 3.3. Structural analysis by x-ray tomography (CT)

Pore size distributions in the range of 250 to 3000 µm were carried out by X-ray CT. This method facilitates a quantitative analysis of porous materials in a non-invasive way [8]. Investigations were conducted on 40x40x150 mm sized test-samples. We used 400 angles for 3D-reconstructions in order to maximize image sharpness. We observed clear differences in pore size distributions (Fig. 3). Whereas samples w/o additive, with SMK 2101-ORIG and TYPE 6, respectively, exhibit predominantly pore radii between 1250 and 1750 µm, this peak was shifted towards smaller radii of about 1000 µm in sample prepared with SMK 2101-TYPE 29. In comparison, sample SMK 2101-TYPE 29 exhibited an about 2-fold increase in total pore numbers ( $3250 \pm 180$  pores).

### 3.4. Microstructural analysis by scanning electron microscopy (SEM)

Further analyses were conducted on the solid skeleton of the test samples. We used scanning electron microscopy SEM) to determine thicknesses of the partitioning walls between macropores (the sample with SMK 2101-TYPE 29 was not included here). Average wall thicknesses were found to be between 55 and 77 µm, with sample SMK 2101-TYPE 6 showing a trend towards thinner intersecting walls. However, the process of sample preparation may result in artifacts. Therefore, presented results must be regarded as estimated.

Table 3

PARTITIONING WALL THICKNESS ACCORDING TO SEM-MEASUREMENTS OF SAMPLES W/O ADDITIVE, WITH SMK 2101-ORIG, SMK 2101-TYPE 6.

	Partitioning wall thickness (MW ± SD) [µm]	Number of samples (N)
w/o additive	$76,9 \pm 69,1$	15
SMK 2101-ORIG	$69,5 \pm 37,9$	21
SMK 2101-TYPE 6	$54,9 \pm 21,2$	30

## 4. Conclusions

The material microstructure of AAC is characterized by its solid microporous matrix and macropores. Macropores are formed during the aluminum-driven expansion of the slurry, whereas micropores (or gel-pores) result from the packing of tobermorite plates and are located within the partition walls between the macropores [9]. We suppose that the high number of macropores with radii from 20–50 µm found in samples TYPE 6 and TYPE 29 coincide with primary pores formed by isolated aluminum particles. Our assumption can be explained with reference to general mechanisms of foam stability. From a thermodynamical point of view, foams (like a wet AAC mix) are unstable due to their high specific surface areas, when compared to gas and liquid in separate states. A durable, fine pore structure indicates stabilization as degradation mechanisms (interlamellar gas diffusion, coalescence, Ostwald-

ripening) are decelerated [10]. According to the Young–Laplace equation (equation 4) stabilisation is achievable upon reduction of the surface tension. In the present study, this stabilization was achieved by the surfactant-character of organosilicon compounds SMK 2101-TYPE 6 and TYPE 29.

Equation 4. Young-Laplace equation.

$$p = 2\sigma/r$$

p – Laplace-pressure [ $\text{N/mm}^2$ ],

$\sigma$  – surface tension [ $\text{N/mm}$ ],

r – radius of the bubble [mm].

Our findings account for the low thermal conductivities observed in samples SMK 2101-TYPE 6 and -TYPE 29. Slightly thinner partitioning walls (TYPE 6) should affect heat transport in the solid matrix and, thus, contribute to the small  $\lambda$ -value. We tend to exclude changes in heat transfer via gas-phase, as observed microstructural differences were predominantly in the macroporous range (Knudsen-number  $<< 1$ ). In conclusion, we suggest that observed reductions in thermal conductivities were invoked by a reduction of heat transfer by radiation. Our assumption is in good agreement with findings by the Forschungsinstitut für Wärmeschutz, FIW (München, Germany). Finite element calculations revealed that the radiation-term of the total heat transport in light weight AAC is close to zero for a mean pore diameter  $\leq 50$  µm. The corresponding reduction of the total thermal conductivity was calculated to be 6,3%.

## Bibliography

- [1] Narayanan N., Ramamurthy K., 2000. Structure and properties of aerated concrete: a review. *Cem. Concr. Comp.* **22**, 321–329.
- [2] Kreft O., Schoch T., 2010. Alitinform. The Influence Of Moisture On The Thermal Conductivity Of AAC. **1 (13)**, 60-65.
- [3] Tran L., Strahlungseffekte bei instationären Heizdraht-messungen an porösen Wärmedämmstoffen. Dissertation. TU Bergakademie Freiberg, Germany, 2002.
- [4] Bave G., Aerated light weight concrete-current technology. In: Proceedings of the Second International Symposium on Lightweight Concretes. London, 1980.
- [5] YTONG Multipor Mineraldämmplatte, European Technical Approval ETA05/0093 (valid through May 8, 2015)
- [6] Zürn S.G., Einfluss der Sandminerale auf die Bildung von Calciumsilikathydraten (C-S-H-Phasen), das Gefüge und die mechanischen Eigenschaften von Porenbetonprodukten. Dissertation. Ludwig-Maximilians-Universität München, Logos Verlag Berlin, 1997.
- [7] Prim P., Witmann F.H., Structure and water absorption of aerated concrete. In: Wittmann F. H., editor. *Proceedings Autoclaved Aerated Concrete, moisture and Properties*. Elsevier, Amsterdam. 43–53, 1983.
- [8] Caty O., 2008. Modelling the properties of closed-cell cellular materials from tomography images using finite shell elements. *Acta Materialia*. **57**, 5524-5543
- [9] Alexanderson J., 1979. Relations between structure and mechanical properties of autoclaved aerated concrete. *Cem. Concr. Res.* **9 (4)**, 507-514
- [10] Myers D., Surfaces, Interfaces And Colloids. Principles and Applications (2ed., Wiley-VCH, New York, 1999.